

Alzheimer's A β (1-40) Amyloid Fibrils Feature Size-Dependent Mechanical Properties

Zhiping Xu,[†] Raffaella Paparcone,[†] and Markus J. Buehler^{†‡§*}

[†]Laboratory for Atomistic and Molecular Mechanics, Department of Civil and Environmental Engineering; [‡]Center for Computational Engineering; and [§]Center for Materials Science and Engineering, Massachusetts Institute of Technology, Cambridge, Massachusetts

ABSTRACT Amyloid fibrils are highly ordered protein aggregates that are associated with several pathological processes, including prion propagation and Alzheimer's disease. A key issue in amyloid science is the need to understand the mechanical properties of amyloid fibrils and fibers to quantify biomechanical interactions with surrounding tissues, and to identify mechanobiological mechanisms associated with changes of material properties as amyloid fibrils grow from nanoscale to microscale structures. Here we report a series of computational studies in which atomistic simulation, elastic network modeling, and finite element simulation are utilized to elucidate the mechanical properties of Alzheimer's A β (1-40) amyloid fibrils as a function of the length of the protein filament for both twofold and threefold symmetric amyloid fibrils. We calculate the elastic constants associated with torsional, bending, and tensile deformation as a function of the size of the amyloid fibril, covering fibril lengths ranging from nanometers to micrometers. The resulting Young's moduli are found to be consistent with available experimental measurements obtained from long amyloid fibrils, and predicted to be in the range of 20–31 GPa. Our results show that A β (1-40) amyloid fibrils feature a remarkable structural stability and mechanical rigidity for fibrils longer than ≈ 100 nm. However, local instabilities that emerge at the ends of short fibrils (on the order of tens of nanometers) reduce their stability and contribute to their disassociation under extreme mechanical or chemical conditions, suggesting that longer amyloid fibrils are more stable. Moreover, we find that amyloids with lengths shorter than the periodicity of their helical pitch, typically between 90 and 130 nm, feature significant size effects of their bending stiffness due to the anisotropy in the fibril's cross section. At even smaller lengths (≤ 50 nm), shear effects dominate lateral deformation of amyloid fibrils, suggesting that simple Euler-Bernoulli beam models fail to describe the mechanics of amyloid fibrils appropriately. Our studies reveal the importance of size effects in elucidating the mechanical properties of amyloid fibrils. This issue is of great importance for comparing experimental and simulation results, and gaining a general understanding of the biological mechanisms underlying the growth of ectopic amyloid materials.

INTRODUCTION

Amyloid fibrils are highly ordered nanoscale assemblies of protein protofibrils that result from densely packed parallel β -sheet structures (Fig. 1). They play a crucial role in the initiation and progression of various neurodegenerative disorders, including Alzheimer's disease, Parkinson's disease, type 2 diabetes, and transmissible spongiform encephalopathies (1). The amyloid state of proteins is universally accessible to a great diversity of amino acid sequences through the conversion from their soluble functional states into highly organized fibrillar aggregates. X-ray diffraction patterns, experimental imaging, and many other experimental investigations have shown that amyloid fibrils feature an extensive β -sheet structure formed by fibrilized polypeptides, stabilized by a dense network of backbone hydrogen bonds (H-bonds) (2–4). Moreover, amyloid fibrils share a common characteristic interstrand twist angle that strongly contributes to the stability of the overall structure and has been theoretically and experimentally investigated (3,5–11). Amyloids have also been discussed as an example of a highly ordered, hierarchical protein material that combines elasticity, sturdiness, and resistance with the ability to provide self-assembling

and self-healing properties (12–15). These properties, combined with a relatively high stability even in adverse chemical environments (16), may also make them good candidates for novel nanobiomaterial applications (17–19). For example, they could be used as nanowires and self-assembled nanostructures (20), natural adhesives (21), or functional templates for biomaterials (13). The potential applications of these supramolecular assemblies could go beyond those of synthetic polymers because amyloid fibrils can provide well-defined structural features and biological functionality in addition to excellent mechanical properties (22,23). A rigorous mechanical characterization of amyloid materials is crucial for such applications, and to elucidate the stabilizing mechanism of amyloid fibrils against structural, thermal, chemical, and mechanical perturbations from a pathological point of view—for example, to understand prion propagation processes and derive statistical links between Alzheimer's disease and type 2 diabetes (24).

Atomic force microscopy (AFM)-based nanoindentation experiments can provide quantitative measurements of local elasticity because they allow the imaging of individual fibrils and the application of forces ranging from piconewtons to nanonewtons. Recent studies have reported values of Young's moduli ranging from a few tens of megapascals (25–27) to several tens of gigapascals (28–30), depending

Submitted November 4, 2009, and accepted for publication December 21, 2009.

*Correspondence: mbuehler@MIT.EDU

Editor: Ruth Nussinov.

© 2010 by the Biophysical Society
0006-3495/10/05/2053/10 \$2.00

doi: 10.1016/j.bpj.2009.12.4317

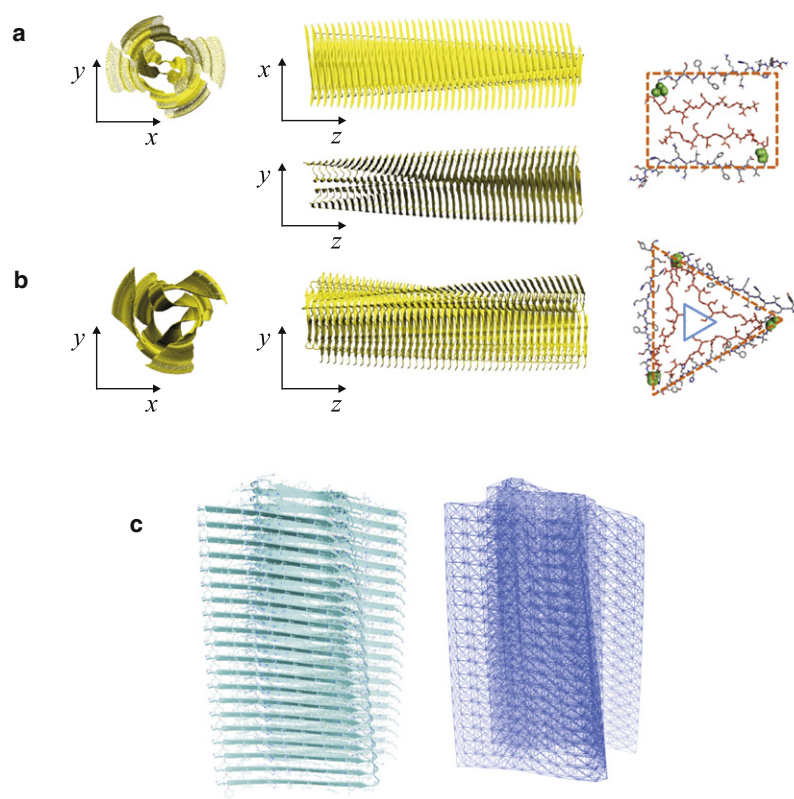


FIGURE 1 Structure of twofold (a) and threefold (b) symmetric assemblies of $A\beta(1-40)$ amyloid fibrils. Both structures have an intrinsic twist along the fibril axis (10,36). In the twofold fibril, two β -strands align in parallel and form a close contact, whereas in the threefold fibril, a hydrophobic core nanopore is formed in the center of the triangular structure. The visualizations on the outermost right show the geometry of a single protofibril layer for each morphology. (c) Full-atomistic and corresponding ENM representations of a twofold symmetric amyloid fibril.

on the size of the considered protein structure (25,29), the experimental approach, and specific loading conditions used (26,30). However, the lack of a detailed mechanical characterization at the atomistic scale (with molecular-level insight into deformation mechanisms), and the relatively large variation in the measured values of Young's moduli of amyloid fibrils have left two major issues unresolved: 1), the effect of boundary conditions and the coupling of deformation modes; and 2), the validity of the model used to extract the mechanical properties.

In AFM measurements, for example, when tensile or bending load is applied to a specific region of amyloid fibrils, the strain energy may be localized spatially at the point where the loading is applied. In addition, at finite deformation, modes such as tension, bending, and twisting can be coupled with one another, and thus the relation between applied stress and measured displacement may not be used directly to extract accurate stiffness measurements, due to the lack of a well-defined stress and strain state.

AFM-based nanoindentations rely on an indirect evaluation of the elastic properties based on stress-strain relations obtained from some type of beam model (e.g., from Euler-Bernoulli theory (25–30)). It is typically based on the assumption of pure bending states while neglecting contributions from rotation and shear. Furthermore, the contact area between the AFM tip or the nanoindenter and amyloid fibril resides at the nanometer scale that is comparable to the characteristic length scale of helical pitch in amyloid fibrils (on the order of 100 nm) as well as the cross section (a few nano-

meters). At such a low aspect ratio, rotational and shear deformations, the anisotropy of the cross section, and the helical geometry may have a significant effect on the bending rigidity of amyloid fibrils.

It is critical to resolve both of these issues to develop a rigorous relationship among amyloid fibril structures, their mechanical properties, and their pathological or physiological functions. To that end, we propose a novel approach to evaluate the structural stability and mechanical parameters of amyloid fibrils by analyzing their normal modes. In normal-mode analyses of proteins, the low-frequency modes of proteins are identified. They typically correspond to collective modes that are related to rigid-body motions and continuum-like deformations (31–34). For proteins with a fibrous structure, these low-frequency modes resemble basic mechanical deformations, such as twisting, transverse bending, and stretching. By utilizing continuum mechanics models, one can use the frequencies of these deformation modes to identify key mechanical material parameters, such as the torsional modulus G , bending rigidity D , and Young's modulus Y (35). Most importantly, the normal-mode-based approach makes it possible to analyze the intrinsic mechanical properties without the adverse effects of specific mechanical boundary conditions or the limited timescales accessible in direct molecular-dynamics simulations.

In this work, we systematically investigate the size dependence of the mechanical properties of amyloid fibrils by using atomistic and continuum finite element-based normal-mode analyses combined in a scheme as shown in

Fig. S1 of the [Supporting Material](#). The use of multiple methods in our study, from atomistic to continuum, is critical to cover the relevant length scales from nanometers to micrometers. We begin by summarizing the key materials and methods used, including the atomic structure of amyloid fibrils, and details about the computational methods utilized. We then proceed with a discussion of the results, and conclude with a broader perspective on the impact of our results on amyloid science and related fields.

MATERIALS AND METHODS

Atomic structure of A β (1-40) amyloid fibrils

For this study, we focus on two polymorphous atomic structures of amyloid fibrils: the twofold symmetric and threefold symmetric A β (1-40) amyloid fibril morphologies. The notation A β (1-40) is used here to indicate the 40 amino acids comprising the fibril. For both the two- and threefold symmetric structures, the atomic geometries of the A β (1-40) amyloid fibrils were constructed from monomer protofibrils as described previously (10,36). These studies provided us with the key geometric parameters, such as the inter-strand distance d and the twist angle θ , that facilitate the construction of A β (1-40) amyloid fibrils with arbitrary lengths, as shown in Fig. 1. These structures served as input geometries for the normal-mode analysis, atomistic simulations, and finite element model development.

The twofold symmetric A β (1-40) amyloid fibril structure consists of two symmetric β strands that form separate β sheets in a double-layered, cross- β motif. The two protofilaments aggregate in the fibril growth direction and possess a helical symmetry along the axis, as shown in Fig. 1 *a*. The cross section of the fibril is approximated as a rectangle with a height of 2.87 nm and a width of 4.67 nm, where the cross-sectional area $A = 13.70 \text{ nm}^2$. As a result of the organized interstrand H-bonds, the protofibrils are closely packed and form layered structures. The threefold symmetric A β (1-40) amyloid fibril consists of three β -strands that form separate β -sheets in a triangular cross- β motif. The three protofibrils also aggregate in the fibril growth direction and possess a helical symmetry along the axis. The fibril cross section can be represented as an equilateral triangle with an edge length of 6.47 nm. The cross-sectional area $A = 18.146 \text{ nm}^2$. In contrast to the side contacts found in twofold symmetric fibrils, the threefold symmetric fibril has a hydrophobic hole in the center; thus, the structure is geometrically constrained, which reduces the contact between the protofibrils. The optimized distances and twist angles between adjacent protofibrils were calculated to be $d = 0.482 \text{ nm}$ and $\theta = 1.29^\circ$ (twofold symmetric structure), and $d = 0.485 \text{ nm}$ and $\theta = 2.12^\circ$ (threefold symmetric structure) (10,36).

The interstrand distance d can also be used to calculate the length of fibril $L = N_{\text{layer}}d$, where N_{layer} is the number of protofibril layers in an amyloid fibril. The aspect ratio n can thus be defined as the ratio between the amyloid fibril length L and the characteristic dimension of the cross section, such as the longer edge length of 4.67 nm in the twofold symmetric structure, and the equilateral edge length of 6.47 nm in the threefold symmetric structure.

Elastic network model

To simulate the mechanical properties of amyloid fibrils based on atomistic-level structure information at relatively large length scales, we used the elastic network model (ENM), which was originally proposed by Tirion (37) and later extended by Hinsen and colleagues (38,39). Here we use the formulation of the ENM as defined by Hinsen (38). The interactions between atoms are smoothly cut off above 10 Å (37). As shown in previous studies (31–34), the lower-frequency normal modes calculated from the ENM describe experimental measurements or standard empirical force-field simulations with good agreement. These modes are collective and correspond to large-amplitude movements and conformational changes of

proteins. A representation of the ENM model is shown in Fig. 1 *c*. Further details are included in the [Supporting Material](#).

Normal-mode analysis

The ENM is widely used in normal-mode analysis of large protein molecules because of the linear elastic nature of the springs that connect the atoms and the resulting computational efficiency. It should be noted that if full-atomistic, conventional force-field methods were to be used, the resulting normal-mode analysis would quickly become computationally intractable. In that case, only very short amyloid fibrils with rather few layers would be accessible to the computational analysis, which would preclude investigation of the size effects of mechanical parameters at scales of up to tens of nanometers and beyond.

The normal modes of a molecular assembly are calculated by diagonalizing the second derivative of the potential energy (Hessian matrix). The eigenvalues of the mass-weighted Hessian matrix give the frequencies of corresponding modes, and the corresponding eigenvectors represent the mode shapes. For macromolecules such as A β (1-40) amyloid fibrils, the first six modes are the rigid-body modes with zero frequencies (including three translation and three rotation modes) (31–34). Most of the next-higher modes (all modes are ranked by the eigenvalues from low to high) with low frequencies are collective modes that typically correspond to elastic deformations such as twisting, bending, and stretching. Although it is rather simple, the ENM model provides an accurate representation of small-deformation (linear elastic) mechanical behavior, as characterized by the collective modes with low frequencies (see also earlier studies using a similar approach (31–34)). Further details are included in the [Supporting Material](#).

Extraction of elastic properties

The normal-mode decomposition of macromolecular motions provides a specific frequency and stiffness for each mode, and thus offers direct information about the elastic properties of an amyloid fibril. Provided that the collective motion of the amyloid fibrils corresponds directly (or closely) to the deformation modes assumed in a continuum model, the parameters extracted from a normal-mode analysis can be related to the elastic constants (such as the Young's modulus) in a continuum model (31–34). Further details are included in the [Supporting Material](#).

Visualization of normal modes

The twisting, bending, and stretching modes of amyloid fibrils are quite distinct from other modes with spatially localized deformation, and thus can be easily picked out. Mechanical deformation modes can be characterized by visualizing the solved mode shape through the associated atomic movement trajectory. To visualize the normal-mode shapes in structural space, the displacement field (i.e., the eigenvectors of the Hessian matrix) x_{in} on atom i for mode n is added to the atom position x_{i0} at equilibrium with a phase factor $A \sin(\alpha)$ (where α varies continuously from $-\pi$ to π). The amplitude A_{ni} is determined to obtain an average root mean-square displacement of 3 Å at phase $\pi/2$ and $-\pi/2$. The Visual Molecular Dynamics (VMD) program (40) is used for visualization of data. The new cartoon representation of the secondary structure is read from the equilibrium structure of amyloid fibrils for each system considered.

Compressive wave-front tracking simulations

We perform all-atom simulations of propagation of a compressive shock wave through the amyloid fibrils to obtain elastic parameters for the finite-element model and additional validation of the ENM results. This represents a direct approach to measure the elastic modulus of amyloid fibrils. The overall simulation approach and integration of different techniques are summarized in Fig. S1. By tracking the wave-front position (i.e., the boundary that separates the deformed and undeformed regions) as a function of

time, we determine the group speed of the propagating wave. In the computational shock experiments, we first equilibrate the system at 300 K for 200 ps (we have confirmed that longer equilibration times do not affect the wave propagation dynamics). One end of the fibril (containing two protofibril layers) is constrained against axial displacement, and a constant velocity shock pulse is applied at the other end (and to the two constrained protofibril layers). As illustrated in Fig. 2 *a*, the pulse is applied by given a constant velocity $v_0 = 100$ m/s to the α -carbon (C_α) atoms in the protofibrils (different shock velocities v_0 from 10 m/s to 1000 m/s are used, and have not been found to affect the wave propagation speed). The constant-velocity compression is maintained for 4 ps of simulation time, during which the shocked end of the protofibrils moves downward by 0.4 nm. We then remove the constant-velocity constraint at the shocked end of the amyloid fibril and constrain its motion along fibril axis to facilitate tracking of the compressive wave propagation (Fig. 2 *b*). Once it is nucleated, the wave front travels at the speed of a longitudinal elastic wave, c . The elastic properties can be extracted based on $Y = c^2\rho$, where Y is the Young's modulus and ρ is the mass density of the fibril. All tracking simulations are performed using an NVT ensemble with $T = 300$ K (Nosé-Hoover thermostat), with a time step of 1 fs. We employ the CHARMM19 all-atom energy function and an effective Gaussian model for the water solvent (41,42) to facilitate rapid sampling of structural configurations (43).

For the twofold (with $L = 19.28$ nm) and threefold (with $L = 29.1$ nm) symmetric amyloid fibrils, we obtain a group speed $c = 4000$ m/s and 3860 m/s, which correspond to Young's modulus values of $Y = 27.24$ GPa and 26.50 GPa, respectively. We find that the sound speed values are rather similar for the two- and threefold fibrils. This suggests that the dense H-bond network within the fibril (with a similarly layered structure in both symmetries) is responsible for the mechanical energy transfer during wave propagation. We note that the Young's moduli values correspond well to earlier experimental measurements (several tens of gigapascals) of the elastic modulus of amyloid fibrils (28–30).

Finite-element analysis of the bending rigidity

Measurements based on the ENM model are limited by the system size that scales with the number of atoms, limiting fibril lengths to ~ 30 nm. To reach scales comparable to or larger than the characterized helical pitch length in amyloid fibrils (on the order of 100 nm), and to capture the size dependence of mechanical properties associated with this length scale, we carry out finite-element analyses.

This approach allows us to capture the rotational and shear contributions to the bending mode at small aspect ratios, and the effects of helical symmetries in amyloid fibrils with fibril length less than the helical pitch length. Because of the one-dimensional nature of amyloid fibrils, an isotropic elastic

fiber model with Young's modulus E (obtained from wave-front tracking (WFT) simulations as described above) and a Poisson's ratio of $\nu = 1/3$ (following the analysis in del Mercato et al. (44)) is chosen. We use rectangular and equilateral triangular cross sections that reflect the geometrical parameters of the corresponding atomistic structures, for both the two- and threefold symmetric fibril morphologies. Three-dimensional solid elements C3D8I are used to discretize the amyloid fibril. In the normal-mode analysis, the vibrational frequencies are calculated via the linear perturbation module in ABAQUS using a Lanczos solver. The results for eigenfrequencies are substituted into expressions from Euler-Bernoulli theory to obtain the nominal bending rigidity, D (elastic properties other than the bending rigidity are not considered here).

RESULTS AND DISCUSSION

To obtain a complete picture of the mechanical properties of amyloid fibrils and their dependence on the geometry, an integrated study using the methods outlined above is carried out, with a focus on the dependence of the mechanical properties on the fiber length, cross-sectional morphology, and intrinsic helical symmetry. As an overview, visualizations of the normal-mode shapes are shown in Figs. 3 and 4 for the two- and threefold symmetric structures, for different fibril lengths. Table S1 summarizes the normal-mode shapes and the ordering of A β (1–40) amyloid fibrils for the two- and threefold symmetric structures. Table S2 summarizes vibrational frequencies with different modes, and Table S3 provides an overview of the mechanical parameters associated with each mode. Movies S1, S2, S3, S4, S5, S6, S7, and S8 show visualizations of the twisting, bending, and stretching modes for the two- and threefold symmetric fibrils.

Twisting modes

The lowest-order mode for the shortest twofold symmetric structure considered here, (with 20 layers or corresponding to ≈ 10 nm length), is a twisting mode as visualized in Fig. 3 and shown in Table S1. The twisting mode turns into the second- and third-lowest modes as the length of

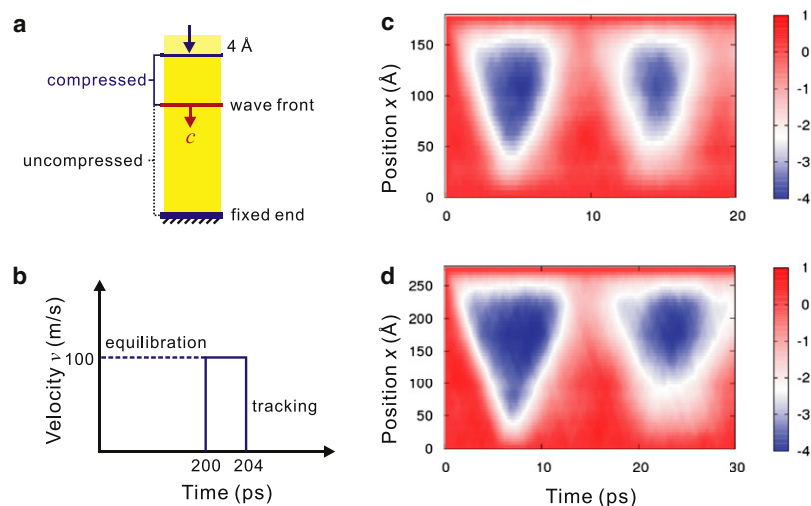


FIGURE 2 Compressive WFT approach carried out using full-atomistic simulations. (a) Compression load is applied by prescribing a constant velocity to the C_α atoms in the two top protofibril layers. (b) Loading history, consisting of an equilibration process for 200 ps, a pulse compression process with constant velocity applied to two top protofibril layers, and a wave-tracking process. (c) Displacement of C_α atoms in the twofold symmetric fibrils (length $L = 19.28$ nm), resulting in a measured wave speed of 4000 m/s. The color describes the axial displacement of the C_α atoms as a function of time (x -axis) and their initial positions (y -axis). (d) Displacement of C_α atoms in the threefold symmetric fibrils (length $L = 29.1$ nm), resulting in a measured wave speed of 3860 m/s.

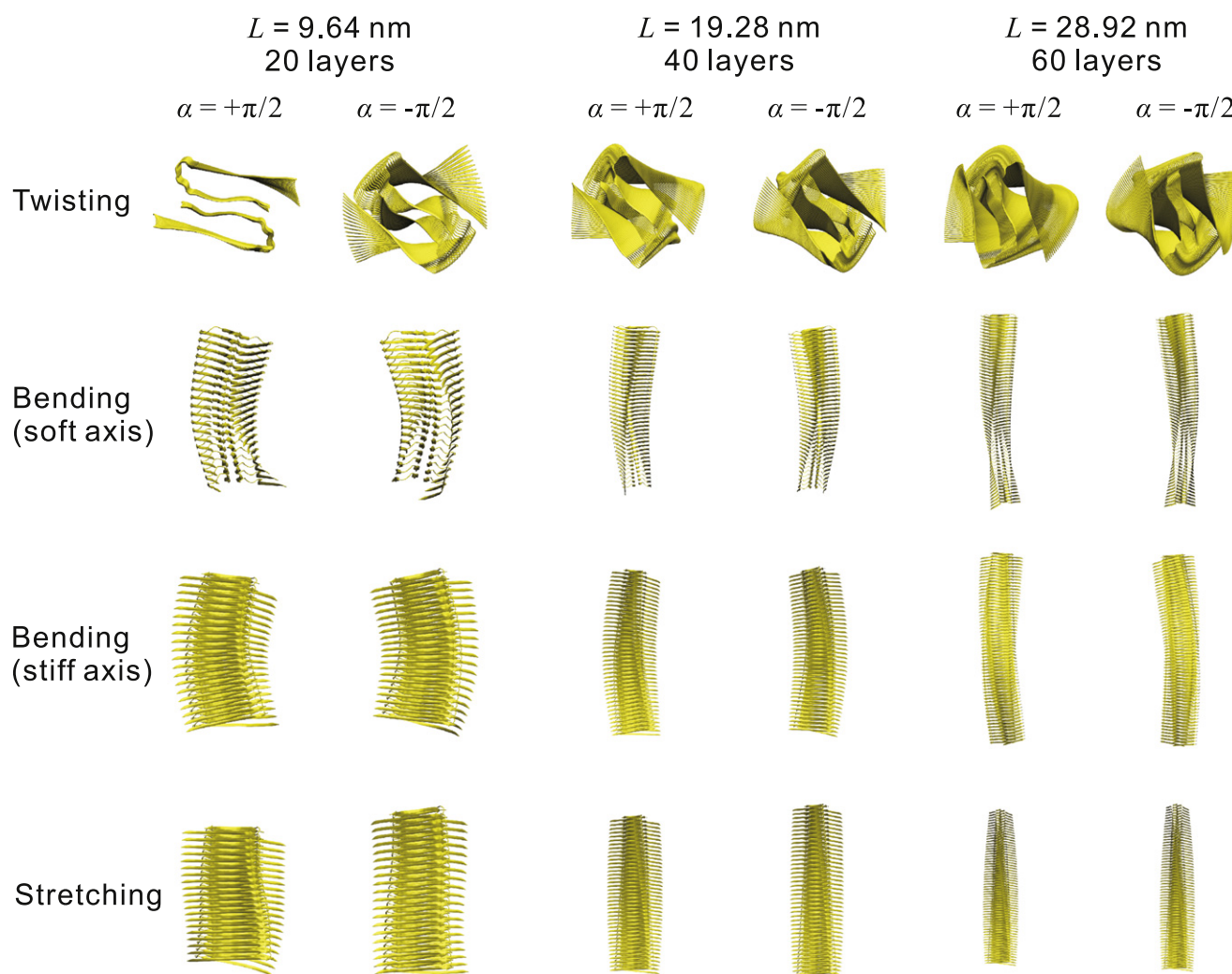


FIGURE 3 Lowest-order collective modes of twofold symmetric amyloid fibrils, including twisting, bending along different axes (soft and stiff), and stretching modes. For shorter fibrils, the soft and stiff axes are well defined, showing significant differences between the two bending modes (where the one with lower frequency corresponds to bending around the soft axis). We find that there is also a significant coupling within these modes, particularly in bending and stretching.

the fibril is increased, when bending modes take the place of the lowest-order modes. The shortest threefold symmetric fibril considered here does not show a distinct first-order twisting mode (as explained in detail further below), which only emerges when longer fibrils are considered, as in the 40- and 60-layer systems (with ≈ 20 nm and/or ≈ 30 nm length; see results in Fig. 4 and Table S1). In these two cases, the twisting modes are the third-lowest mode observed, with two bending modes taking the place of the lowest two modes.

The corresponding torsional modulus G calculated from Eq. S4 ranges from 5.19 to 5.83 GPa, and is found to be an increasing function of the fibril length L . Fig. 5 *a* reports the torsional modulus G as a function of the fibril length for both two- and threefold symmetric morphologies. The increase in G is more pronounced in the twofold symmetric structure. Notably, we find that the increase of the torsional

modulus G saturates quickly as the fibril length exceeds 20 nm, suggesting that these boundary effects quickly disappear for this mode of deformation as the length is increased.

Based on a detailed analysis of the mode shapes of short fibrils with both two- and threefold symmetry, we find that there exist localized deformations at the open ends in the fibrils. This implies that the protofibrils at the ends are more weakly bound to the rest of the amyloid fibrils, and as a result could begin to disassociate relatively easily under mechanical or chemical perturbation from environment. This applies in particular to the threefold symmetric fibrils, where a hydrophobic core nanopore is formed in the center of the triangular structure (as shown in Fig. 1 *b*), and thus the contact between protofibrils is looser than in the twofold symmetric fibrils. This results in an overall reduced stability of this fibril morphology. In agreement with this notion, the

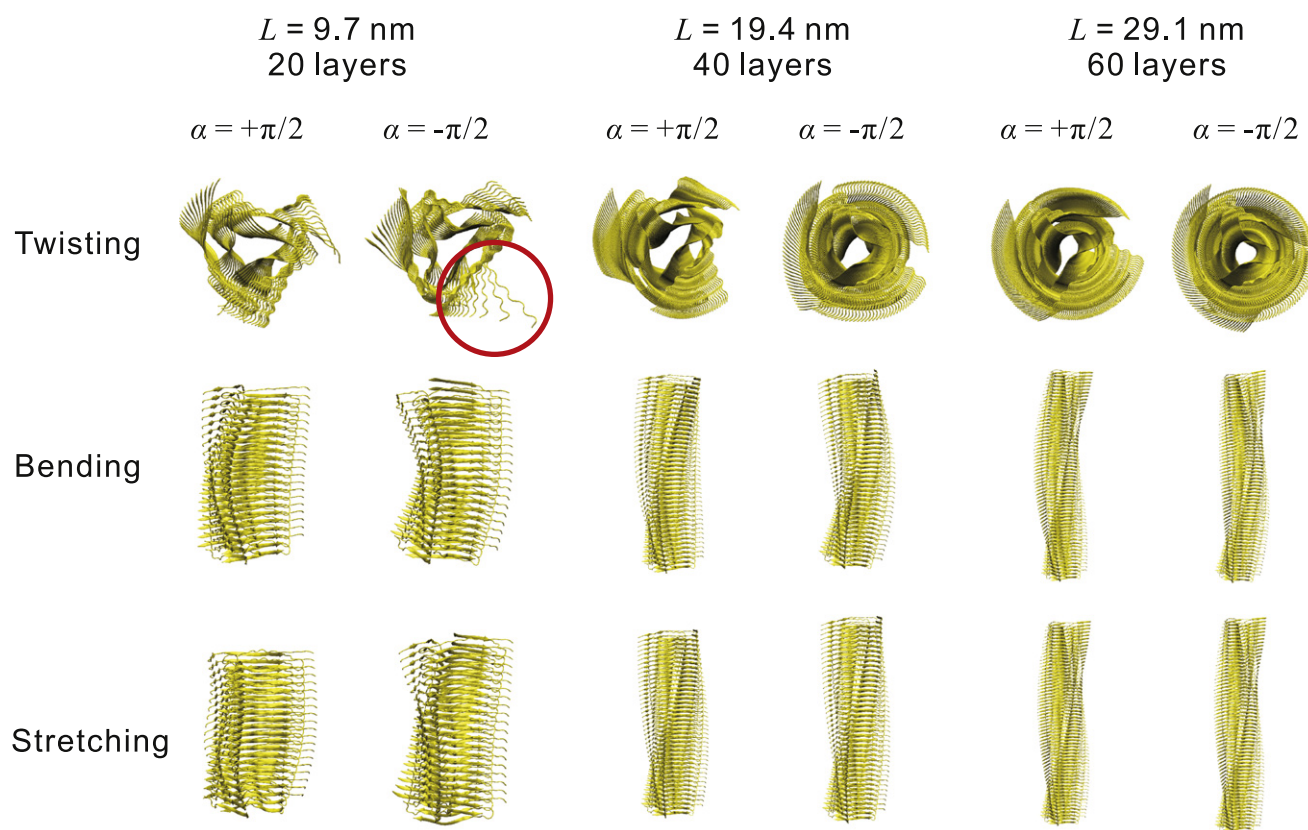


FIGURE 4 Lowest-order collective modes of threefold symmetric amyloid fibrils, including twisting, bending, and stretching modes. The threefold symmetric triangular symmetry of the cross section results in a degenerated transverse bending mode.

lowering of geometric constraints also gives rise to a series of radial breathing modes with low frequencies for short fibrils, (such as the 9th–12th modes for the 20-layer fibril, as shown in Table S1). We observe that these modes are strongly coupled to the first-order twisting mode. As a result, the torsional modulus cannot be extracted in this case (and the mode shape of the second-order twisting mode is instead represented in Fig. 4). This twisting mode also shows a strong localization at the fibril ends, suggesting an enhanced disassociation probability of the threefold symmetric structure, as discussed in previous reports (30).

Transverse bending modes

We now turn to the transverse bending modes and focus first on the twofold symmetric fibril. Since the twofold symmetric amyloid fibril has a rectangular cross section, as shown in Fig. 1 *a*, it possesses two distinct nondegenerate bending axes that correspond to two different eigenfrequencies and thus mode shapes (as can also be directly confirmed in the visualizations shown in Fig. 3). As a result, there exist two distinct bending stiffnesses depending on the axis of bending. The axis that gives the smaller moment of inertia for bending is referred to as the “soft” axis, and the other one is referred to as the “stiff” axis for bending.

The results summarized in Fig. 5 *b* show that the resulting bending rigidity D depends strongly on the fibril length L . Furthermore, the values obtained from our model are consistent with the experimentally measured values (in the range of 10^{-26} – 10^{-25} Nm²) (28,30). Due to the intrinsic twist along the fibril axis, the anisotropy of the cross section is expected to disappear once the fibril length is much larger than the helical pitch length L_p (when the twist angle accumulated along the fibril axis is much larger than 2π), that is, $L_p \approx 130$ nm for two-fold symmetric fibrils, and $L_p \approx 82$ nm for three-fold symmetric fibrils (10,36). This means that even though there exists a length-dependent anisotropy in the bending rigidity, it is expected to disappear for very long fibrils. The applicability of ENM for relevant length scales, however, is prohibited by the limitation of computational power.

To overcome this limitation, we perform finite-element analyses that enable us to reach much larger length scales and directly test this hypothesis. Fig. 6 *a* shows the finite-element model setup, depicting a model without and with twisting. These models are chosen to test the hypothesis that the twisted geometry indeed results in the emergence of a single bending rigidity once a critical length scale is reached. Fig. 6 *b* shows example results from the normal-mode analysis for these two models, for different lengths. Fig. 6 *c* shows

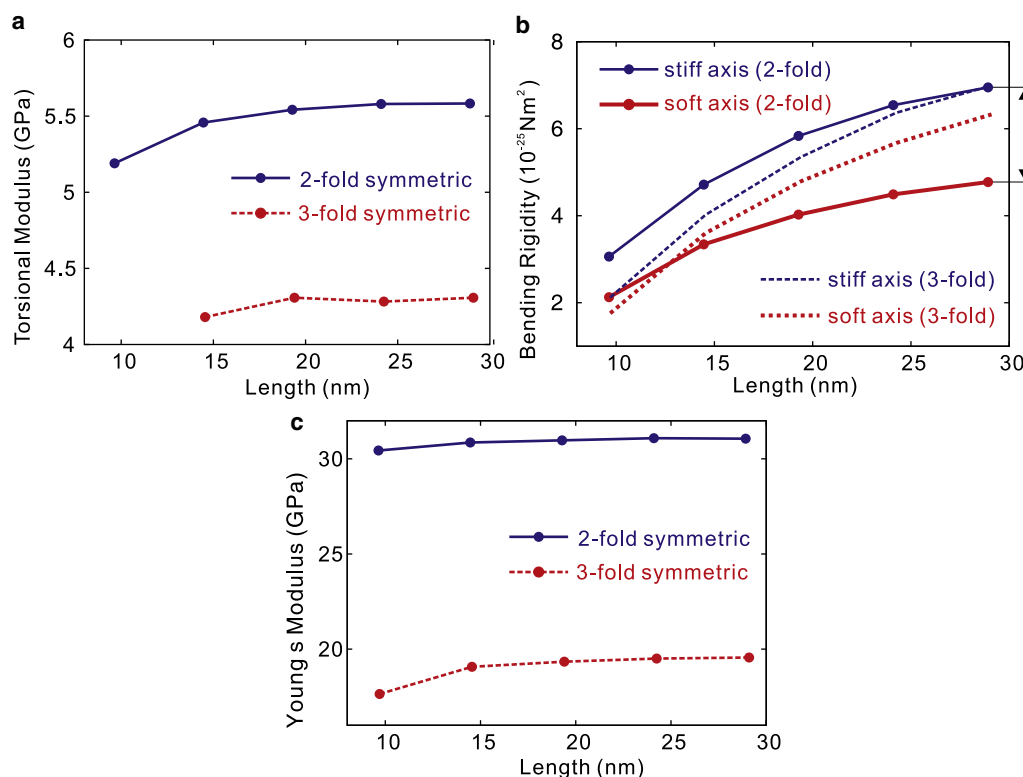


FIGURE 5 Elastic properties of amyloid fibrils as a function of length L , as obtained from ENM calculations. (a) Torsional modulus G . (b) Bending rigidity $D = YI$ along the soft and stiff axes of two- and threefold symmetric amyloid fibrils (with smaller and larger moments of inertia, respectively). (c) Young's modulus Y . All parameters are shown as a function of the amyloid fibril length up to ≈ 30 nm.

the bending rigidities for both models and for both the soft and stiff bending axes. The results confirm that once the fibril length is larger than the helical pitch length, the difference between soft mode and stiff mode disappears in twisted fibrils, but remains in untwisted fibrils. In agreement with our hypothesis, the rigidity of the long, twisted fibril lies between the two limits for untwisted amyloid fibrils. Furthermore, we observe that the nominal bending rigidities show a size-dependent bending rigidity for aspect ratios below a critical aspect ratio of $n^* \approx 10$. This is because at such small aspect ratios, the rotational and shear effects that are neglected in the Euler-Bernoulli theory, which assumes pure bending deformation, become important for $n < 10$. Altogether, the critical aspect ratio n for Euler-Bernoulli theory validity, and the helical pitch length L_p in the fibrils define two critical length scales that characterize the size-dependent bending behavior of amyloid fibrils. Specifically, our analysis shows that relatively simple rod models can only be applied to amyloid fibrils whose length exceeds L_p .

We now briefly focus on the bending properties of the threefold symmetry amyloid fibril. Due to the symmetric triangular cross section of the threefold symmetric fibril (see Fig. 1 b), the bending rigidities measured from our normal-mode analysis are very close to one another. This can be confirmed by comparing the values reported in

Fig. 5 b, which shows that as the length of amyloid fibrils approaches ≈ 30 nm, the two obtained bending rigidities approach the same value of $6.3 \times 10^{-25} \text{ Nm}^2$. As discussed above, this behavior is in contrast to the twofold symmetric fibril, where a significant deviation of the bending stiffnesses around the soft and stiff axes is observed.

Longitudinal stretching modes

As shown in Fig. 5 c, the Young's modulus Y is calculated to be 30–31 GPa for the twofold symmetric fibril, and 19–20 GPa for the threefold symmetric fibril, which is on the same order of previous experimental measurements (2–24 GPa) (28–30). For the longitudinal stretching mode in twofold symmetric fibrils, we find that there exists a significant coupling with bending modes along the soft axis, as shown in Fig. 3. The narrow distribution of Young's modulus values as a function of the fibril length suggests that less significant boundary effects exist in this deformation mode in comparison with the twisting modes. Therefore, the application of stretching and compression modes represents a more reliable method to extract elastic properties even from relatively small structures (however, boundary effects due to the application of tensile or compressive load may still play an important role and must be carefully considered).

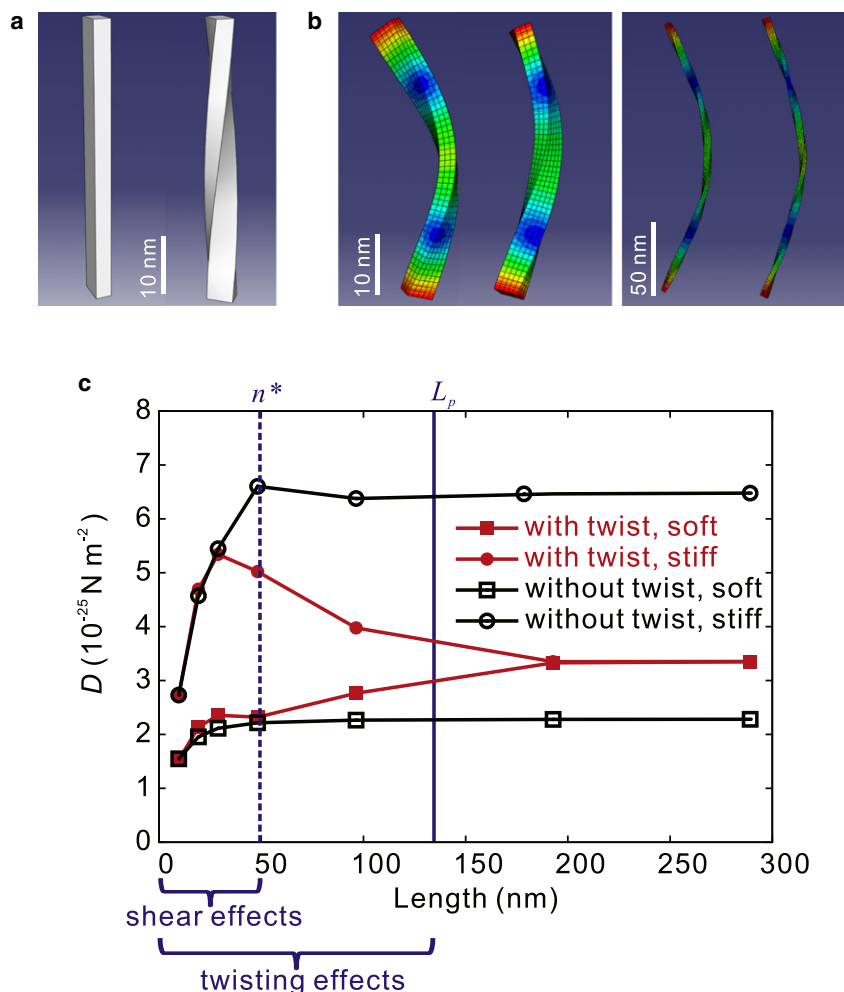


FIGURE 6 Results of normal-mode analysis based on three-dimensional, finite-element simulations. (a) The geometry of untwisted and twisted amyloid fibrils (length $L = 48.2$ nm (100 layers)). (b) The shape of bending modes along soft and stiff axes, respectively (for fibril lengths $L = 48.2$ nm (100 layers) and $L = 192.8$ nm (400 layers)). The bending modes for longer fibrils illustrate the degeneracy of the soft and stiff modes. The color represents displacement amplitude, scaled up by a factor of 80 for visualization. (c) Bending rigidity D of twofold symmetric amyloid fibrils with (solid symbols) and without (open symbols) the intrinsic twist along the fibril axis. The length-dependent bending rigidity values show significant size effects resulting from two distinct mechanisms: 1), at low aspect ratios $n < n^* = 10$, the bending rigidities calculated based on the Euler-Bernoulli theory increase with fibril length because of the unaccounted-for contributions from rotational and shear effects (for details, see [Supporting Material](#)); and 2), there is a geometric effect from the intrinsic twist on the resulting bending properties. For the untwisted fibril, the bending rigidities associated with the soft and stiff modes converge to distinct constant values for larger L . For twisted fibrils, when L is larger than the helical pitch length L_p , the difference between the soft and stiff modes disappears and their bending rigidity approaches the same value.

Higher-order modes

The normal modes with frequencies higher than the first-order twisting, bending, and stretching modes discussed above correspond to higher-order collective modes and those with localized deformation in the fibril. Some of the characteristic modes that can be related to continuum deformations are summarized in [Table S1](#).

CONCLUSIONS

In this work, we used ENM-based normal-mode analysis, full-atomistic simulations, and finite-element analysis to investigate the mechanical properties of $A\beta(1-40)$ amyloid fibrils. The use of normal-mode analysis enabled us to exclude ambiguous effects that result from the application of loading and boundary conditions. We find that the aspect ratio and helical pitch length of the fibrils determine two critical size-dependent length scales, below which the presenting shear stress or low bending rigidity along the soft axis will reduce its mechanical resistance. The size dependence and enhancement of the structural stability and associated mechanical properties for long amyloid fibrils revealed

here may imply a pathological consequence. Furthermore, our study also clarifies the validity of mechanical models to extract the mechanical properties of nanoscale helical fibrils from experiments or atomistic simulations by achieving a physical stress/strain state and applying the appropriate model at various length scales.

Specifically, for short fibrils ($L < 10$ nm for twofold and $L < 15$ nm for threefold fibrils), large-amplitude displacement at the open ends (twofold fibrils) and radial breathing motion (threefold fibrils) play a significant role, leading to structural instabilities. Under perturbations in environments such as thermal fluctuations, pH value changes, or solvent flow, the protofibrils at the ends may disassociate from the rest of the structure.

For long amyloid fibrils, a remarkably enhanced structural stability was observed. The torsional modulus G and Young's modulus Y are well defined: $G \approx 5.5$ and 4.3 GPa for twofold symmetric and threefold symmetric $A\beta(1-40)$ amyloid fibrils, respectively, and $Y \approx 31$ and 20 GPa, respectively. The higher stiffnesses in the twofold fibril are due to its close contact within protofibrils and denser structure. The bending rigidity (in the range of $2-7 \times 10^{-25} \text{ N m}^2$), however, shows

TABLE 1 Comparison of key mechanical properties of amyloid fibrils with other materials

Material	Torsional/shear modulus (GPa)	Bending rigidity (10^{-25} Nm ²)	Young's modulus (GPa)
Twofold A β (1-40) amyloid fibril (ENM, this work)	4.3	2.1–4.8	31.0
Threefold A β (1-40) amyloid fibril (ENM, this work)	5.6	1.8–6.3	20.0
Twofold A β (1-40) amyloid fibril (WFT, this work)	-	-	27.2
Threefold A β (1-40) amyloid fibril (WFT, this work)	-	-	26.5
Amyloids (simulation) (28)	-	-	4–40
Amyloid fibrils (experimental)	0.3 (30)	0.1–2.5 (28–30)	12–17 (28–30)
Spider silk (45)	2.38	-	10–30
Steel (46)	80	-	200
Concrete (46)	-	-	18–30
Glass (46)	5–24	-	17–90

a significant size dependence because of both the rotational/shear contributions at low aspect ratios and the effect of the helical symmetry along the fibril axis. This size dependence is prominent for the structures investigated in this work and will be significant for fibrils with either a small aspect ratio or length L smaller than the helical pitch length L_p , which is on the order of 100 nm. The threefold fibril optimizes its resistance to bending loads by utilizing a more isotropic cross section. Full-atomistic, molecular-dynamics simulations based on the wave-tracking method result in a rather similar value of the Young's modulus close to 27 GPa, which is well defined here by the elastic dynamics. Additional finite-element analysis results based on this value elucidated the validity of a one-dimensional continuum model for amyloid fibrils at lengths larger than the periodicity defined by their intrinsic twist, $L > L_p$.

The elastic parameters identified here, such as the torsional and Young's moduli, lay the foundation for understanding the mechanical properties of amyloid fibrils. Specifically, our results suggest that amyloids are extremely stiff nanostructures in comparison with engineering materials such as concrete, glass, and steel, and other biological structural materials such as spider silk (Table 1). In addition, amyloid fibrils feature an intrinsic self-assembling ability and a remarkable propensity to change conformation, controlled by external cues (22). The coupling between different deformation modes (e.g. tension/compression and rotation) is an interesting feature of amyloid fibrils, which has also been observed in recent full atomistic simulations (47).

We note that the ENM approach used here is limited by both the nature of the normal-mode analysis and the simplicity of the model. The normal-mode analysis uses the second energy derivatives matrix, which is calculated based on the equilibrium structure. Thus, the perturbation nature of the analysis is only reasonable for small-amplitude harmonic motions, and prohibits large-amplitude motion and nonlinear mechanisms, such as fracturing of the amyloid fibrils with breaking or reforming of the H-bond network. Furthermore, in the ENM, the simple exponential decaying function (given in Eq. S1) may not correctly reflect the huge stiffness difference ($r_k = k_c/k_H$) between covalent bonds in backbone and H-bonds (here defined as the distance between donor

and acceptor atoms, for example, between oxygen and nitrogen atoms in a C=O...H-N H-bond). A revised ENM with correct stiffness levels inside proteins could be implemented to obtain more accurate results (and with an explicit treatment of slip planes associated with potential failure mechanisms of H-bonded β -sheet structures).

SUPPORTING MATERIAL

Eight movies, methods, one figure and three tables are available at [http://www.biophysj.org/biophysj/supplemental/S0006-3495\(10\)00085-8](http://www.biophysj.org/biophysj/supplemental/S0006-3495(10)00085-8).

The authors thank Professor Marc Delarue's group (Institut Pasteur, France) for providing the ENMsolver NOMAD-Ref for the normal-mode analysis.

This work was supported by the Office of Naval Research, Defense Advanced Research Projects Agency, MIT Energy Initiative, and National Science Foundation. The authors declare no conflict of interest of any sort.

REFERENCES

- Chiti, F., and C. M. Dobson. 2006. Protein misfolding, functional amyloid, and human disease. *Annu. Rev. Biochem.* 75:333–366.
- Dobson, C. M. 2005. An overview of protein misfolding diseases. In *Protein Folding Handbook*. J. Buchner and T. Kiefhaber, editors. Wiley-VCH Verlag GmbH & Co. KGaA, Weinheim, Germany. 1093–1113.
- Jiménez, J. L., E. J. Nettleton, ..., H. R. Saibil. 2002. The protofilament structure of insulin amyloid fibrils. *Proc. Natl. Acad. Sci. USA*. 99:9196–9201.
- Nelson, R., and D. Eisenberg. 2006. Recent atomic models of amyloid fibril structure. *Curr. Opin. Struct. Biol.* 16:260–265.
- Harper, J. D., C. M. Lieber, and P. T. Lansbury, Jr. 1997. Atomic force microscopic imaging of seeded fibril formation and fibril branching by the Alzheimer's disease amyloid- β protein. *Chem. Biol.* 4:951–959.
- Ionescu-Zanetti, C., R. Khurana, ..., A. L. Fink. 1999. Monitoring the assembly of Ig light-chain amyloid fibrils by atomic force microscopy. *Proc. Natl. Acad. Sci. USA*. 96:13175–13179.
- Goldsbury, C. S., J. Kistler, ..., G. J. Cooper. 1999. Watching amyloid fibrils grow by time-lapse atomic force microscopy. *J. Mol. Biol.* 285:33–39.
- Bauer, H. H., U. Aebi, ..., H. P. Merkle. 1995. Architecture and polymorphism of fibrillar supramolecular assemblies produced by in vitro aggregation of human calcitonin. *J. Struct. Biol.* 115:1–15.
- Periole, X., A. Rampioni, ..., A. E. Mark. 2009. Factors that affect the degree of twist in β -sheet structures: a molecular dynamics simulation study of a cross- β filament of the GNNQQNY peptide. *J. Phys. Chem. B*. 113:1728–1737.

10. Paparcone, R., and M. J. Buehler. 2009. Microscale structural model of Alzheimer A β (1-40) amyloid fibril. *Appl. Phys. Lett.* 94:243904.
11. Buchete, N. V., R. Tycko, and G. Hummer. 2005. Molecular dynamics simulations of Alzheimer's β -amyloid protofilaments. *J. Mol. Biol.* 353:804–821.
12. Gelain, F., D. Bottai, ..., S. Zhang. 2006. Designer self-assembling peptide nanofiber scaffolds for adult mouse neural stem cell 3-dimensional cultures. *PLoS One*. 1:e119.
13. Scheibel, T., R. Parthasarathy, ..., S. L. Lindquist. 2003. Conducting nanowires built by controlled self-assembly of amyloid fibers and selective metal deposition. *Proc. Natl. Acad. Sci. USA*. 100:4527–4532.
14. Zhang, S. 2003. Fabrication of novel biomaterials through molecular self-assembly. *Nat. Biotechnol.* 21:1171–1178.
15. Zhang, S., T. Holmes, ..., A. Rich. 1993. Spontaneous assembly of a self-complementary oligopeptide to form a stable macroscopic membrane. *Proc. Natl. Acad. Sci. USA*. 90:3334–3338.
16. Zurdo, J., J. I. Guijarro, ..., C. M. Dobson. 2001. Dependence on solution conditions of aggregation and amyloid formation by an SH3 domain. *J. Mol. Biol.* 311:325–340.
17. Hamada, D., I. Yanagihara, and K. Tsumoto. 2003. Engineering amyloidogenicity towards the development of nanofibrillar materials. *Trends Biotechnol.* 22:93–97.
18. MacPhee, C. E., and C. M. Dobson. 2000. Chemical dissection and reassembly of amyloid fibrils formed by a peptide fragment of transthyretin. *J. Mol. Biol.* 297:1203–1215.
19. MacPhee, C. E., and D. N. Woolfson. 2004. Engineered and designed peptide-based fibrous biomaterials. *Curr. Opin. Solid State Mater. Sci.* 8:141–149.
20. Reches, M., and E. Gazit. 2003. Casting metal nanowires within discrete self-assembled peptide nanotubes. *Science*. 300:625–627.
21. Mostaert, A. S., M. J. Higgins, ..., S. P. Jarvis. 2006. Nanoscale mechanical characterisation of amyloid fibrils discovered in a natural adhesive. *J. Biol. Phys.* 32:393–401.
22. Cherny, I., and E. Gazit. 2008. Amyloids: not only pathological agents but also ordered nanomaterials. *Angew. Chem. Int. Ed.* 47:4062–4069.
23. LeDuc, P. R., and D. N. Robinson. 2007. Using lessons from cellular and molecular structures for future materials. *Adv. Mater.* 19:3761–3770.
24. Meersman, F., and C. M. Dobson. 2006. Probing the pressure-temperature stability of amyloid fibrils provides new insights into their molecular properties. *Biochim. Biophys. Acta*. 1764:452–460.
25. Graveland-Bikker, J. F., I. A. T. Schaap, ..., C. G. de Kruif. 2006. Structural and mechanical study of a self-assembling protein nanotube. *Nano Lett.* 6:616–621.
26. Guo, S., and B. B. Akhremtchev. 2006. Packing density and structural heterogeneity of insulin amyloid fibrils measured by AFM nanoindentation. *Biomacromolecules*. 7:1630–1636.
27. Del Mercato, L. L., P. P. Pompa, ..., R. Rinaldi. 2007. Charge transport and intrinsic fluorescence in amyloid-like fibrils. *Proc. Natl. Acad. Sci. USA*. 104:18019–18024.
28. Knowles, T. P., A. W. Fitzpatrick, ..., M. E. Welland. 2007. Role of intermolecular forces in defining material properties of protein nanofibrils. *Science*. 318:1900–1903.
29. Kol, N., L. Adler-Abramovich, ..., I. Rouso. 2005. Self-assembled peptide nanotubes are uniquely rigid bioinspired supramolecular structures. *Nano Lett.* 5:1343–1346.
30. Smith, J. F., T. P. J. Knowles, ..., M. E. Welland. 2006. Characterization of the nanoscale properties of individual amyloid fibrils. *Proc. Natl. Acad. Sci. USA*. 103:15806–15811.
31. Krebs, W. G., V. Alexandrov, ..., M. Gerstein. 2002. Normal mode analysis of macromolecular motions in a database framework: developing mode concentration as a useful classifying statistic. *Proteins*. 48:682–695.
32. Delarue, M., and Y. H. Sanejouand. 2002. Simplified normal mode analysis of conformational transitions in DNA-dependent polymerases: the elastic network model. *J. Mol. Biol.* 320:1011–1024.
33. Tama, F., and Y. H. Sanejouand. 2001. Conformational change of proteins arising from normal mode calculations. *Protein Eng.* 14:1–6.
34. Tama, F. 2003. Normal mode analysis with simplified models to investigate the global dynamics of biological systems. *Protein Pept. Lett.* 10:119–132.
35. Weaver, W. J., S. P. Timoshenko, and D. H. Young. 2001. *Vibration Problems in Engineering*. Wiley-Interscience, Hoboken, NJ.
36. Paparcone, R., J. Sanchez, and M. J. Buehler. 2009. Comparative study of polymorphous Alzheimer's A β (1-40) amyloid nanofibrils and microfibers. *J. Comput. Theor. Nanosci.* doi:10.1166/jctn.2010.1481. In press.
37. Tirion, M. M. 1996. Large amplitude elastic motions in proteins from a single-parameter, atomic analysis. *Phys. Rev. Lett.* 77:1905–1908.
38. Hinsen, K. 1998. Analysis of domain motions by approximate normal mode calculations. *Proteins*. 33:417–429.
39. Hinsen, K., A. Thomas, and M. J. Field. 1999. Analysis of domain motions in large proteins. *Proteins*. 34:369–382.
40. Humphrey, W., A. Dalke, and K. Schulten. 1996. VMD: visual molecular dynamics. *J. Mol. Graph.* 14:33–38.
41. Lazaridis, T., and M. Karplus. 1997. "New view" of protein folding reconciled with the old through multiple unfolding simulations. *Science*. 278:1928–1931.
42. Lazaridis, T., and M. Karplus. 1999. Effective energy function for proteins in solution. *Proteins*. 35:133–152.
43. Paci, E., and M. Karplus. 2000. Unfolding proteins by external forces and temperature: the importance of topology and energetics. *Proc. Natl. Acad. Sci. USA*. 97:6521–6526.
44. del Mercato, L. L., G. Maruccio, ..., R. Rinaldi. 2008. Amyloid-like fibrils in elastin-related polypeptides: structural characterization and elastic properties. *Biomacromolecules*. 9:796–803.
45. Frank, S. K., K. Ko, ..., J. W. Song. 2004. *Engineering Properties of Spider Silk Fibers*. Kluwer Academic Publishers, Dordrecht.
46. Shackelford, J., W. Alexander, and J. Park. 1995. *CRC Practical Handbook of Materials Selection*. CRC, Boca Raton, FL.
47. Paparcone, R., S. Keten, and M. J. Buehler. 2010. Atomistic simulation of nanomechanical properties of Alzheimer's A β (1-40) amyloid fibrils under compressive and tensile loading. *J. Biomechanics*. 43:1196–1201.